On Improving Navigation Accuracy of GPS/INS Systems

Dorota Grejner-Brzezinska, Charles Toth, and Yudan Yi

Abstract

Direct georeferencing, also referred to as direct platform orientation (DPO), is defined as direct measurement of the imaging sensor external orientation parameters (EOP), using positioning and orientation sensors, such as the Global Positioning System (GPS) and Inertial Navigation System (INS) or Inertial Measurement Unit (IMU). Imaging sensors, most frequently supported by the DPO technique, are digital cameras, lidar systems, multi-spectral or hyper-spectral scanners, or interferometric synthetic aperture radar (INSAR). While for scanning sensors the use of DPO is compulsory, frame digital cameras can also directly benefit from this modern technique of sensor orientation. With direct sensor orientation, the requirement for ground control, tie-point matching and aerotriangulation (AT) is significantly reduced, or even entirely eliminated, resulting in shorter times of data acquisition and processing, and streamlined and highly automated data workflow and quality control. Most of the time, the requirement for ground control points is limited to periodic system calibrations and quality control check. Direct georeferencing is considered a fundamental technology of conventional mobile mapping systems (MMS).

Despite significant progress in GSP/INS-based direct georeferencing technology in the last decade, there is still room for improvement in terms of better accuracy and better tolerance to GPS outages. This paper is focused on three error modeling and compensation techniques that could potentially improve GPS/INS system's performance on both land-based and airborne platforms: (1) extended gravity compensation, (2) IMU signal de-noising, and (3) stochastic modeling of IMU errors.

Introduction

Integration of GPS and inertial navigation techniques is the primary means for direct platform orientation (DPO), providing high-accuracy timing, positioning and attitude information of the imaging sensor(s) mounted either on a land-based or airborne platform, thus forming a mobile mapping system (MMS). Real-time or post-processing of GPS/IMU data directly provide image georeferencing in a selected mapping coordinate system. Oriented images are then used in various photogrammetric processes to extract thematic and topographic information, such as terrain data, natural and man-made objects, etc. These features with their positional information and additional attributes can then be directly transported to a GIS database, or converted to a digital map. Also, with the increasing use of multi-sensor mapping or intelligence-collecting platforms, data fusion has become a crucial step in the design of these systems and an essential component of spatial data processing algorithms.

The fundamental step of any data integration process is georeferencing or geometric fusion of data (time-space registration), provided by the Global Positioning System (GPS) and Inertial Navigation System (INS) or Inertial Measurement Unit (IMU): GPS/IMU or GPS/INS. Clearly, georeferencing by fusion of GPS and inertial technology is the back-bone of any modern mobile mapping system, and substantial research effort has been devoted to extensive algorithmic developments, performance analysis and practical implementations of GPS/IMU or GPS and dead-reckoning systems (Bossler *et al.*, 1991; Schwarz *et al.*, 1993; Bossler and Toth, 1995; El-Sheimy *et al.*, 1995; Skaloud *et al.*, 1996; Abdullah, 1997; Grejner-Brzezinska, 1997; Toth and Grejner-Brzezinska, 1998; Grejner-Brzezinska 1999; El-Sheimy and Schwarz, 1999; Mostafa *et al.*, 2000; Mostafa and Hutton, 2001). Most of the publications to date in the mapping and navigation communities are focused on integrating differential GPS with high-end, navigation-grade IMUs. Since the market price of these systems is still rather high, and the performance of the consumer-grade IMU sensors still does not meet the high accuracy requirements of the majority of mapping projects, the challenge to examine the applicability of lower-end IMU sensors to direct georeferencing, under the assumption that special signal processing algorithms and extended error models are applied, is long overdue. Thus, the primary objective of this paper is to demonstrate several methods for additional improvements in the GPS/INS performance with a special emphasis on the enhancement of stand-alone inertial navigation with medium and low-end IMUs. In addition, we also examined the possibility to improve inertial navigation of the navigation-grade sensors, using an improved gravity compensation procedure (Grejner-Brzezinska and Wang, 1998; Grejner-Brzezinska *et al.*, 2003 and 2004a-b) and careful modeling of the sensor errors. From the MMS perspective, our primary objective is to improve the long-term sensor performance and to achieve better accuracy. This is an ongoing research topic, thus, we do not present any final findings and recommendations yet. Instead, the theoretical foundation of our methods and preliminary test data analysis are provided for different IMU sensors combined with differential GPS in a land-based scenario.

The test data, both static and kinematic, were collected in several survey sessions on the Ohio State University (OSU)

Dorota Grejner-Brzezinska and Yudan Yi are with The Ohio State University, Department of Civil and Environmental Engineering and Geodetic Science, 2070 Neil Avenue, Columbus, OH 43210.

Charles Toth is with The Ohio State University, Center for Mapping, 1216 Kinnear Road, Columbus, OH 43212.

Photogrammetric Engineering & Remote Sensing
Vol. 71, No. 4, April 2005, pp. 377–389.

0099-1112/05/7104–0377/$3.00/0

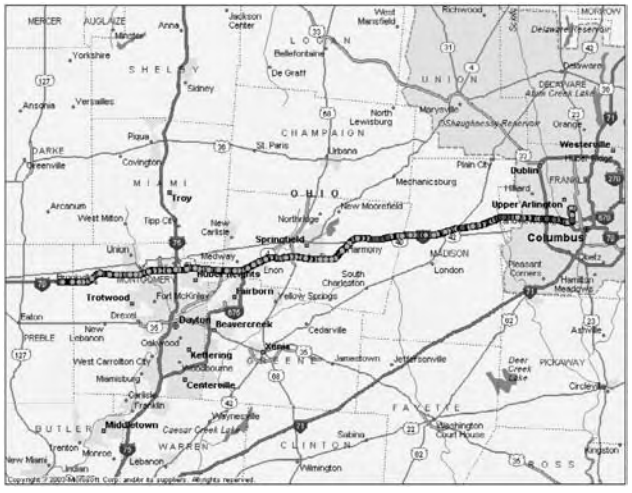

Figure 1. Trajectory of the Columbus – Dayton GPS/IMU experiment; the dark segments indicate the sections used in the free inertial navigation tests.

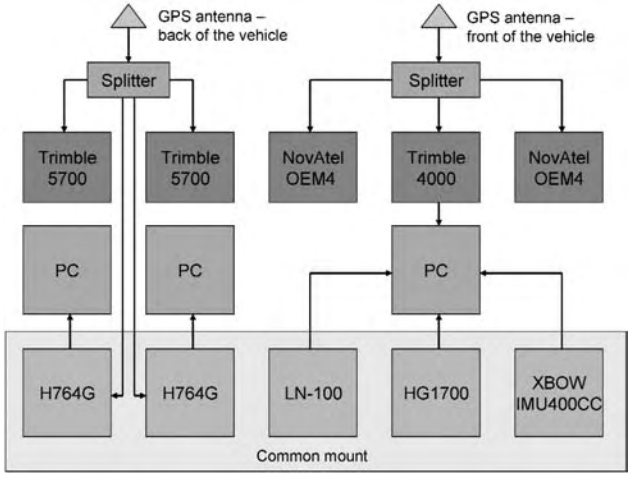

Figure 2. Navigation sensor and data acquisition system configuration of the test MMS vehicle.

Campus and on a 100-mile long highway test in Western Ohio, as depicted in Figure 1 by the dots highlighting the corridor. The mobile mapping system was installed in a GMC Suburban vehicle; the navigation sensors included five different IMUs (two of which were the same model, Honeywell H764G) and five GPS receivers, as shown in Figure 2. The GPS/INS integration software used in the analyses presented here is the OSU-developed AIMS™ system (see Toth and Brzezinska, 1998; Grejner-Brzezinska 1999). The positioning module of this system is based on a tight integration of dual frequency differential GPS carrier phases and raw velocity and angular rates data provided by a navigation grade strapdown LN-100 system from Northrop Grumman Corp. In addition a recently developed module of the AIMS™ software, implementing the loose integration model, was also used and tested in the experiments described here. The current extended AIMS™ configuration consists of LN-100, H764G and HG1700 IMUs from Honeywell, and the micro-electro-mechanical system (MEMS) IMU400CC from Crossbow Technology, Inc. Their characteristics are presented in Table 1.

GPS/INS – Primary Error Sources

Given their fundamental operational differences, GPS and INS are considered complementary positioning techniques. Essentially, GPS is a geometry-based system, with the advantage of long-term position accuracy. Differential GPS that normally removes most of the systematic errors can provide highly accurate centimeter-level position determination providing means for the error estimation of the inertial sensors. Unlike GPS, an INS system is based on the laws of Newtonian physics and is affected by gravity. Errors in inertial navigation are functions of the following factors: (a) initial condition errors including the alignment process, (b) errors in gravitational attraction compensation, (c) errors in coordinate transformation, (d) time-dependent accelerometer and gyroscope errors, (e) errors from external navigation aids used, and (f) errors excited by the dynamics of the vehicle.

Although the long-term accuracy of a stand-alone INS cannot compare to that of GPS, its navigation solution is necessary during times of GPS loss. GPS-calibrated INS provides reliable bridging during GPS outages, and supports the ambiguity resolution after the GPS signals are re-acquired. Thus, the effective navigation error level depends on systematic and random GPS errors as amplified by satellite geometry. The GPS/INS systems based on high-quality inertial systems and supported by differential carrier phase GPS data can reach accuracies of a few centimeters per coordinate

TABLE 1. IMU CHARACTERISTICS ACCORDING TO THE MANUFACTURERS' SPECS

IMU Sensor/Grade	Gyro		Accelerometer	
	Type	Characteristics	Type	Characteristic
LN100 Navigation	Nondithered 18cm Zero Lock™ Laser Gyro	Bias = 0.003°/h Random walk = 0.001°/h$^{1/2}$ Scale factor = 1ppm	Miniature Accelerometer A4	Bias = 25μg Scale factor = 40ppm
H764G Navigation	Dithered GG1320AN RLG	Bias = 0.0035°/h Random walk = 0.0035°/h$^{1/2}$ Scale factor = 5ppm	QA2000	Bias = 25μg Scale factor = 100ppm
HG1700 Tactical	Dithered GG1308 RLG	Bias = 2.0°/h Random walk = 0.125 ~ 0.3°/h$^{1/2}$ Scale factor = 150ppm	RBA500	Bias = 1.0mg Scale factor = 300ppm
IMU400C Consumer	Nondithered Silicon MEMS Gyro	Bias = 1°/sec Random walk = 2.25°/h$^{1/2}$ Scale factor = 1%	Silicon MEMS Accelerometer	Bias = 8.5mg Scale factor = 1%

axis at the flight level (Abdullah, 1997; Grejner-Brzezinska, 1999; El-Sheimy and Schwarz, 1999; Mostafa *et al.*, 2000). Skaloud (2002) lists the achievable attitude accuracy for GPS/INS systems, as a function of the gyro grade, assuming GPS update rates anywhere between 1 and 15 seconds (Table 2). The attitude error characteristics can be decomposed into a time-dependent spectrum; a one-second interval primarily corresponds to the noise, while at 1 to 3 minute period the short-term drifts prevail, which may not be fully observable by GPS, even at a 1-second update rate. In general, the absolute attitude error over longer periods of time (with GPS aiding) depends on the dynamics of the trajectory (i.e., performing maneuvers along the trajectory would improve the gyro bias and heading estimation). The remaining errors include the residual part of the long-term gyro drift, not observable by GPS, the residual short-term gyro drift, and the noise.

The fundamental georeferencing Equation 1, shown here for a lidar sensor, is the primary means of applying the directly determined EOP to transform the measured sensor coordinates to the ground coordinates in the selected mapping frame. The accuracy of the resulting coordinates depends upon a number of factors, such as the sensor placement within the platform, and the imaging sensor and system calibration being among the most important factors, besides the accuracy of the image orientation parameters provided by GPS/INS. While the importance of calibration and its stability was pointed out by many authors (Skaloud, 2002; Grejner-Brzezinska, 2001; Mostafa, 2002), it is also important to analyze and understand the overall performance and limiting factors of the IMU sensors, depending on the type of the sensor, environment and mission design, and the coupling with the gravity field.

$$r_{M,k} = r_{M,INS} + R^{M}_{INS}(R^{INS}_{L} \cdot r_{L} + b_{INS}) \quad (1)$$

where
$r_{M,k}$—3D coordinates of point k in the mapping frame,
$r_{M,INS}$—3D INS coordinates in the mapping frame,
R^{M}_{INS}—rotation matrix between the INS body frame and mapping frame, measured by GPS/INS,
R^{INS}_{L}—boresight matrix between the image sensor frame and INS body frame,
r_{L}—3D object coordinates in laser frame,
b_{INS}—boresight offset component.

State-of-the-art imaging sensors can easily deliver image data in almost any spatial and temporal resolution, and thus the detection of objects, in general, can be sufficiently automated. However, the positioning accuracy of the extracted objects depends much more on the quality of the GPS/INS navigation data as opposed to the quality of acquired imagery, simply because it is based on direct sensor orientation, which has an open-loop characteristic in terms of error modeling (Skaloud *et al.*, 1996). The platform position and attitude data are estimated from physical measurements, which are prone to severe systematic errors in addition to the typical random errors (in conventional practice, ground control presents a feedback for the measurement and estimation process, and thus provides a superior basis for error compensation). Therefore, the error modeling of navigation sensors, as well as the adequate compensation for them is of paramount importance in realizing the ultimate positional accuracy of the objects extracted from the image data, especially where ground control is not utilized.

As synergistic components of an integrated system, GPS and INS work together to account for most of these errors. Namely, GPS calibrates most of the IMU errors on-the-fly, and provides the means for in-flight alignment, while inertial system provides a wide bandwidth and continuous measurements of position, velocity, and orientation. In addition, platform dynamics and carefully planned maneuvers usually allow for the de-correlation of the misalignment errors from other state vector components. There are, however, remaining error sources that cannot be removed by the integration procedure or proper mission conditioning. One example is the high noise level in lower-end IMU sensor signals which requires data pre-processing (de-noising). Similarly, higher-end sensors would also benefit from signal de-noising, even though their effective noise level is much smaller. Another example is insufficient gravity compensation in the strap-down navigation algorithm. Signal de-noising and enhanced gravity compensation together with careful modeling of the stochastic behavior of the IMU sensors are of primary importance in our study. They are the possible sources of improvements in inertial navigation and means of exploring the potential of the lower-end sensors to support direct georeferencing, especially for the land-based MMS applications, where object distances are much shorter, as compared to the airborne systems.

The Problem of Gravity Compensation

Typically, navigation algorithms consider the gravity field to be normal (ellipsoidal), meaning that the deflections of the vertical (DOV), defined as the difference between the actual gravity and the gravity model used, are ignored in the gravity compensation procedure (see Figure 3a). This normally results in the growth of inertial navigation errors with time in the horizontal channels, which is especially detrimental for stand-alone INS operations (see Figure 3b). Several parameters affect the quality of the gravity compensation through the model used and its degree/order of expansion, while the model's quality itself depends on the type, accuracy and spacing of the gravity anomaly data used to create the model, the method of upward continuation, i.e., the physical models and operational techniques used, as well as, the type of approximation adapted in the process. More details on the gravity representation and its impact on the navigation accuracy can be found in (Jekeli, 1997; Kwon, 2004).

TABLE 2. ATTITUDE PERFORMANCE (ACCURACY) BASED ON GPS/IMU INTEGRATION (SKALOUD, 2002); RLG – RING LASER GYRO; FOG – FIBER OPTIC GYRO; DTG – DRY TUNED GYRO

Time Defining the Attitude Error Characteristics	Navigation Grade Sensor (typically, RLG)		Tactical Grade Sensor (typically FOG, DTG)	
	Pitch and Roll [deg]	Heading [deg]	Pitch and Roll [deg]	Heading [deg]
1 s	0.0008–0.0014	0.0008–0.002	0.001–0.02	0.001–0.05
1–3 minutes	0.0014–0.0030	0.0040–0.005	0.005–0.04	0.008–0.10
Absolute-longer time	Same as for 1–3 minutes; maneuver-dependent			

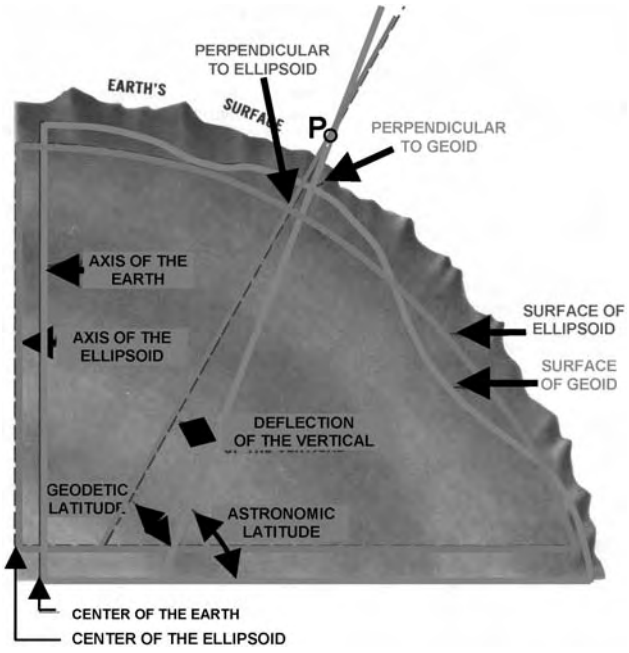

(a)

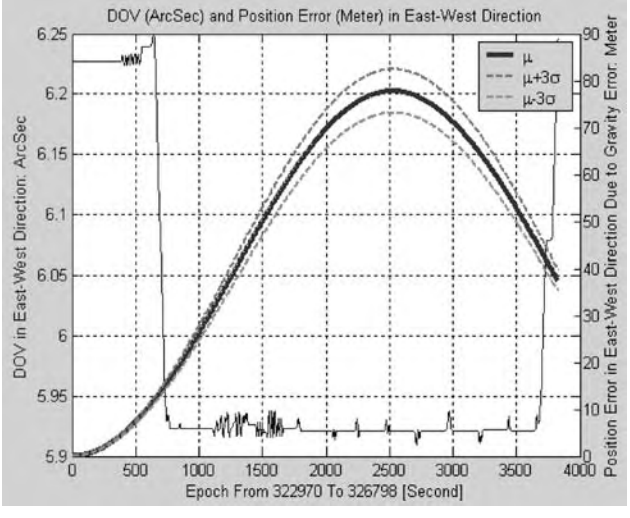

(b)

Figure 3. (a) Deflection of the vertical, DOV, (b) East-West DOV and corresponding position error (mean DOV (μ) was used) bounded by $\pm 3\sigma$ (Grejner-Brzezinska *et al.*, 2004a).

DOV are generally in the order of several arcseconds, except for rugged terrain; the global max/min values of 86/-113 arcsec (ξ, north DOV) and 108/-93 arcsec (η, east DOV) occur in the Himalayan region. In the United States, particularly large DOV occur in the Rocky Mountains and around trench regions (e.g., Hawaii). These are also the areas where the DOV change most rapidly. To limit the navigation error increase, some military systems incorporate active gravity field compensation, such as real-time DOV estimation from models. The horizontal error growth due to gravity field and system noise is much slower than in the vertical channel, and is bound within the 84.4-minute Schuler period. The typical horizontal error growth reaches 0.5–1.0 nm/hr for navigation-grade commercial systems. The vertical channel normally needs an external aid, such as GPS, to control its error growth. A recent discussion on the importance of the gravity compensation in the inertial system performance, from the sensor side, can be found in (Gleason, 2003). Some results reporting the use of DOV data for enhanced gravity compensation in GPS/INS systems are presented in Grejner-Brzezinska and Wang (1998) and Grejner-Brzezinska *et al.* (2003 and 2004a-b).

Inertial navigation follows Newton's second law of motion defined in the inertial (non-rotating) frame (Equations 2.1 and 2.2):

$$\ddot{\bar{x}} = \bar{\mathbf{a}} + \bar{\mathbf{g}}(x) \tag{2.1}$$

$$\bar{\mathbf{g}} = \bar{\mathbf{g}}_m + \Delta\bar{\mathbf{g}} \; and \; \Delta\bar{\mathbf{g}} = \begin{bmatrix} -\mathbf{g}_o\xi \\ -\mathbf{g}_o\eta \\ \Delta\mathbf{g} \end{bmatrix} \tag{2.2}$$

where
$\ddot{\bar{x}}$—the total acceleration vector,
$\bar{\mathbf{a}}$—the acceleration sensed by the accelerometer,
$\bar{x}$—the position vector (therefore, $\ddot{\bar{x}}$ is the acceleration vector),
$\bar{\mathbf{g}}(x)$—the total gravitational acceleration vector,
$\bar{\mathbf{g}}_m$—the gravity model,
$\Delta\bar{\mathbf{g}}$—the difference between the actual gravity and the gravity model used (error in gravity compensation),
$\mathbf{g}_o$—the nominal value of gravity,
ξ and η—north and east components of DOV, respectively,
$\Delta\mathbf{g}$—the gravity disturbance.

The primary observable provided by an accelerometer is the difference between kinematic inertial acceleration and mass gravitation. Thus, errors in the observed accelerations are affected by errors in the gravity model used, translating to the sensor positioning errors, as seen in Equation 3, which represents the time-differential equation for the position error, δx, to the first order due to errors in the system, which is obtained by perturbing Equation 2.1, i.e., by applying the differential operator δ. The resulting navigation errors translate into errors in the coordinates of object points extracted from directly oriented imagery, if a GPS/INS system is used to support camera or lidar systems.

$$\delta\ddot{x} = \frac{\delta g}{\delta x}\delta x + \delta g + \delta a \tag{3}$$

A detailed analysis of the total inertial error dynamics reveals a coupling among the unknowns that, in general, may complicate the navigation solution process (Jekeli, 2001). The errors in DOV enter directly into the horizontal velocity errors in linear combination with the attitude errors. This, generally speaking, makes the parameter separation difficult in the estimation procedure (Grejner-Brzezinska and Wang, 1998). Thus, using DOV in gravity compensation, which introduces less tilt error, leads to reduced coupling of the horizontal accelerations into the vertical axis. Therefore, it can be expected that (high-accuracy) DOV compensation should decrease not only the positioning error, but also improve the attitude determination, which is of great interest in mapping.

To illustrate the effect of different levels of gravity compensation on the positioning results, the simulation of the navigation errors as a function of the gravity model used and the duration of free inertial navigation are presented in Table 3. The gravity models analyzed include the normal (ellipsoidal) model and the EGM96 (degree and order 360), which are compared to the "reference true model," i.e., the GSM (120 harmonics derived from GRACE data combined with 121–360 harmonics from EGM96), which is currently the best available gravity model. The inertial navigation simulator

TABLE 3. SIMULATED FREE INERTIAL NAVIGATION POSITION ERRORS AS FUNCTIONS OF DIFFERENT GRAVITY ERROR MODELS

	Normal versus GSM [m]		EGM96 versus GSM [m]	
Free Inertial Navigation Time [s]	100 m Ellipsoidal Height at 50 km/h	1000 m Ellipsoidal Height at 150 km/h	100 m Ellipsoidal Height at 50 km/h	1000 m Ellipsoidal Height at 150 km/h
30	0.01	0.01	0.00	0.00
60	0.03	0.03	0.00	0.00
300	0.89	0.82	0.01	0.02
600	3.42	2.84	0.05	0.14
1200	10.75	6.16	0.19	0.57

(Kwon, 2004, private communication) used to create Table 3 assumes constant altitude and velocity of the vehicle, and the navigation path along a great circle. The biases, scale factors and white noise of the inertial sensor errors, as well as the gravity disturbances can be selected to investigate the amount of navigation errors coming from a specific component. Two scenarios were simulated based on the trajectory between two points −84.10° Longitude, 39.86° Latitude, and −84.81° Longitude, 39.83° Latitude, with the ellipsoidal heights of 100 m and 1000 m, and velocities of 50 km/hr and 150 km/hr for typical land-based and airborne mobile mapping applications, respectively. The average DOV along the trajectory range between ±5 arcsec in the NE direction and 2–12 arcsec in the EW direction for the EGM model, and 7–4 arcsec in the NE direction and 4–7 arcsec in the EW direction for the GSM model. The selected levels of the IMU sensor errors are as follows: accelerometer bias of 20 μg and gyroscope bias of 0.01°/hr, accelerometer and gyro scale factors of 40 ppm and 5 ppm, respectively; accelerometer and gyroscope white noises of 5 $\mu g/hr^{1/2}$ and 0.001 $°/hr^{1/2}$, respectively, are based on the navigation grade IMU. The errors shown in Table 3 represent the combined effects of the gravity model and the biases/noise coming from the IMU. As expected, errors due to inadequate gravity compensation are rather small as the gravity field in the area is quite smooth, with no significant anomalies. Still, a comparison of the normal gravity with the GSM model indicates several meters of error after a 30-minute navigation period. The residual effect of GSM, as compared to less accurate EGM96, amounts to less than 60 cm after 30 minutes.

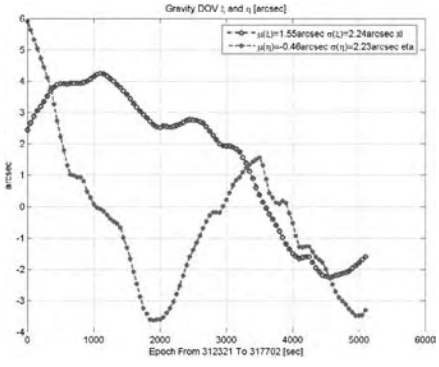

Figure 4. The NGA DOV data for the Ohio test area (corresponds to the trajectory presented in Figure 1).

The Impact of DOV Compensation on Navigation Accuracy

To assess the impact of enhanced gravity compensation, a 3D 2 arc minute by 2 arc minute grid of National Geospatial-Intelligence Agency (NGA) DOV data were used in this study to complement the WGS84 normal gravity model, with the primary objective to determine to what extent accurate gravity information can improve the accuracy of stand-alone inertial navigation during a GPS outage. Since no visible impact of DOV compensation is expected for low-end sensors, only the navigation grade sensors, such as LN-100 and H764G were used in the gravity compensation experiment.

A land-based test dataset collected in Ohio was analyzed (relatively benign set of conditions in terms of an anomalous gravity signal). The true DOV components in both SN and EW directions along the vehicle trajectory were of the order of a few arcseconds only, as shown in Figure 4. The DOV estimates were computed based on the GPS/INS solution by assuming a 1st order Gauss-Markov process for DOV. The comparison of the reference DOV with the Kalman filter estimates indicates a difference in the order of the DOV magnitude. This suggests that the error models used in the Kalman filter and/or correlation among the state parameters could have affected the DOV estimates. Since a substantial effort was put into selecting and tuning the stochastic models (described in a following section), it is most likely that the inseparability of the orientation and gravity errors complicates the DOV and, subsequently, the navigation solutions. Consequently, using known DOV values should allow for more accurate and reliable navigation solution. Naturally, more significant effect would be observed in rugged terrain areas where DOVs are in the order of tens of arcseconds.

The position and attitude differences between the GPS/INS solutions with and without DOV compensation using the LN-100 data are shown in Figures 5 and 6. The differences in positioning due to DOV are at the 1 to 3 centimeter level in

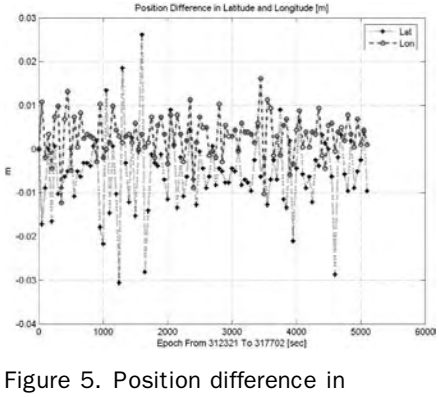

Figure 5. Position difference in latitude and longitude for GPS/INS solutions with and without DOV.

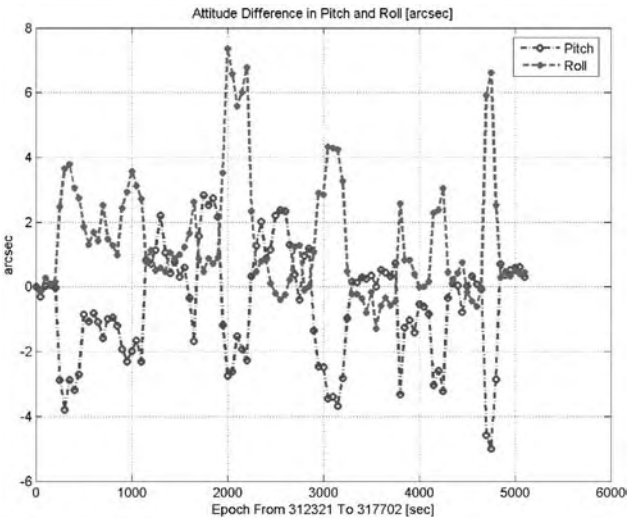

Figure 6. Attitude difference in pitch and roll for GPS/INS solutions with and without DOV.

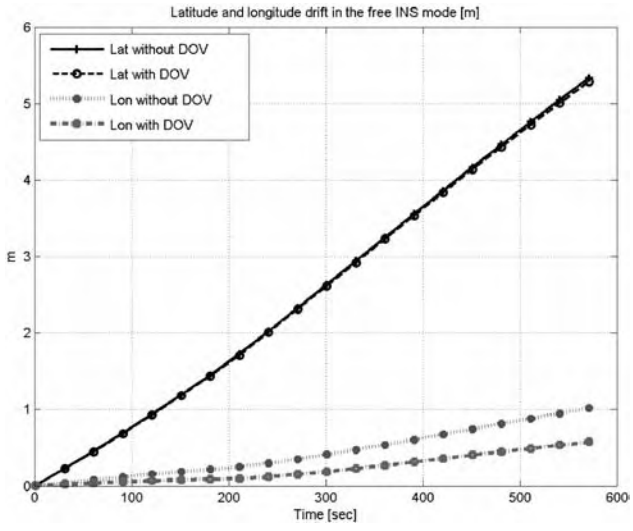

Figure 7. Position drift with and without DOV compensation in free inertial navigation, as compared to the reference GPS/INS solution.

the horizontal components, and, as expected, the impact on height is at the noise level. In general, the magnitude of the attitude differences is comparable to the level of DOV compensation (the main statistics are shown in Table 4). The primary effect of DOV compensation is, however, expected in the free navigation mode, where a clear improvement (as opposed to differences only) should be observed, using the GPS/INS solution as true reference. To estimate the amount of improvement due to DOV compensation, the free-inertial solutions with and without DOV compensation were formed and compared to the reference true solution for a 570-second segment of the trajectory using the LN-100 dataset. Figure 7 indicates that the positioning improvement in the WE direction is significant (approximately 50 percent in the end of the test interval, as compared to the DOV-free solution), while in the NS direction the DOV compensation has no visible impact. In this case it was probably due to the fact that the vehicle was moving in WE direction allowing for limited calibration in the NS direction.

In summary, the results presented here clearly indicate a positive effect of DOV compensation primarily on the horizontal position and attitude components. As expected, the impact of DOV compensation is stronger in the free inertial navigation case. As the test area in Ohio displays small gravity anomaly, GPS/IMU data must be collected over a more rugged terrain, where DOV signal would reach several tens of arcseconds, to further study the effects of DOVs on the inertial navigation accuracy.

TABLE 4. STATISTICS OF ABSOLUTE DIFFERENCES IN POSITION AND ATTITUDE BETWEEN THE GPS/INS SOLUTIONS BASED ON LN100 SENSOR WITH AND WITHOUT DOV COMPENSATION

	Mean	Std	Max	Min	Units
North	7.40	6.49	48.47	0.00	mm
East	4.35	3.37	20.03	0.00	mm
Up	2.61	2.18	11.33	0.00	mm
Heading	3.05	1.48	6.69	0.00	arcsec
Pitch	1.40	1.15	5.17	0.00	arcsec
Roll	1.61	1.74	8.27	0.00	arcsec

IMU Signal De-noising Using Wavelet Decomposition

With a number of low-cost MEMS-based IMU systems available currently on the market, the interest in assessing their applicability to land-based and, to a lesser extent, to airborne direct sensor orientation is growing. However, the low-cost inertial sensors suffer from relatively high measurement noise, which degrades the overall performance of the integrated system, especially during the loss of GPS lock. The IMU signal consists, in general, of true motion dynamics, white noise, vibration disturbances and dither disturbances (for RLG). Thus, the goal of signal de-noising is to remove the noise and the effects of dithering and vibrations, while preserving the spectrum of the motion dynamics.

In terms of error classification, the inertial sensor errors include deterministic and stochastic components. The stochastic errors can be further grouped into color (or time correlated) noise and uncorrelated white noise. Deterministic errors and stochastic color noise can be accounted for using models, either provided by the manufacturer, or derived through the error modeling procedures, discussed in the sequel. However, the white noise cannot be modeled and, therefore, must be reduced or isolated by a smoothing technique, also referred to as signal de-noising.

Signal De-noising Procedure: Overview and Example

The commonly used de-noising techniques include, for example, the moving average and low-pass filtering. Recently, a wavelet-based de-noising technique has been applied to smooth the raw inertial measurements to improve the inertial navigation accuracy and gravity signal recovery from GPS/IMU data (Li and Jekeli, 2004). The fundamental principle of the wavelet-based de-noising technique is the decomposition of the signal contaminated by noise into (a) an approximation, i.e., the low-frequency components of the original signal, and (b) the so-called detail that corresponds to the high-frequency components (Equation 4). For the *n-level* decomposition, there are $n + 1$ possible ways to decompose or encode the signal.

$$\mathbf{s}(t) = \mathbf{a}_k(t) + \sum_{i=1}^{i=k} \mathbf{d}_i(t). \quad (4)$$

In Equation 4, $\mathbf{s}(t)$ represents the original signal, $\mathbf{a}_k(t)$ is the approximation, representing the true signal, including deterministic errors and stochastic colored noise after optimal k-level de-noising, and $\mathbf{d}_i(t)$ corresponds to the details for each level of decomposition (LOD).

It should be mentioned that one of the potential side effects of signal de-noising is the possibility of over-smoothing, which may invalidate some of the predetermined models of deterministic errors and stochastic correlated color noises. The over-smoothing effects could be reduced by a careful selection of the optimal level of decomposition that is a function of the system's dynamics, data sampling rate, type of IMU sensor, etc. To prevent the possible removal of the true dynamics from the signal, the bandwidth of the true motion dynamics must be carefully analyzed together with the spectrum characteristics of the wavelet de-noising algorithm. The maximum allowable LOD is normally determined by examining the statistics (mean, standard deviation auto-correlation sequence, power spectrum, etc.) of the removed noise, as shown next. The wavelet de-noising algorithm used here was derived from the Matlab wavelet toolbox, based on the Symlet wavelets, which are considered near-symmetrical, linear phase filters.

To demonstrate the process of optimal LOD selection, Figures 8 to 11 are analyzed next. Figure 8 illustrates an example of LOD determination through examination of the statistics of the removed noise for a static Crossbow MEMS IMU400CC dataset. As can be observed in Figure 8, the maximum allowable LOD, in this example, is around 11 for both the gyroscope and acceleration signals, based on the deflection point of the standard deviation of the removed noise corresponding to a tolerable mean. Naturally, the maximum LOD is generally smaller in the kinematic case, to prevent the removal of the high frequency dynamic signals, as shown in Figure 9. In this example, the maximum allowable LOD of four for the acceleration and gyroscope raw measurements was inferred. It should be mentioned that in order to derive a full spectrum of allowable LODs for a particular sensor, diverse motion dynamics should be analyzed to select an appropriate LOD for varying portions of the trajectory (i.e., static, moderate dynamics, straight path, turn, etc.).

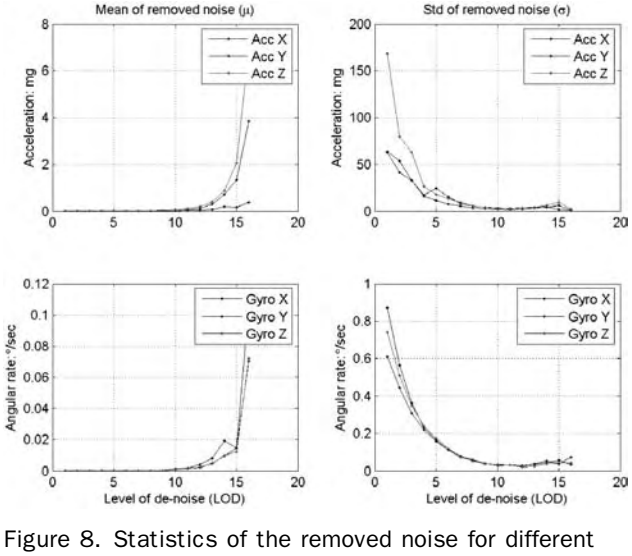

Figure 8. Statistics of the removed noise for different LOD for a static IMU400CC dataset.

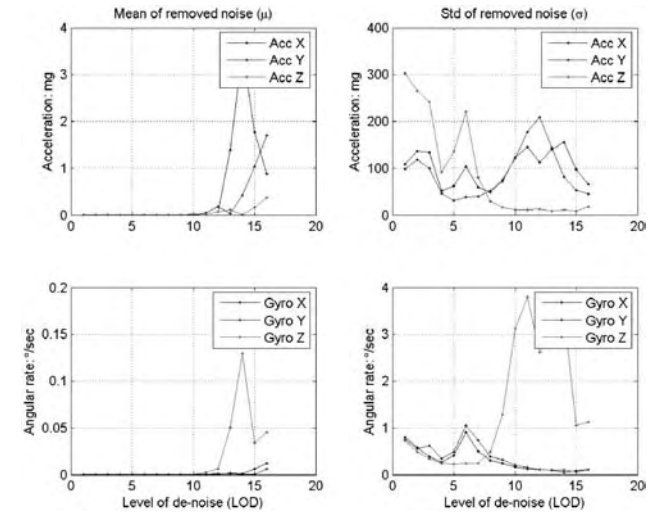

Figure 9. Statistics of the removed noise for different LOD for a kinematic IMU400CC dataset (moderate dynamics).

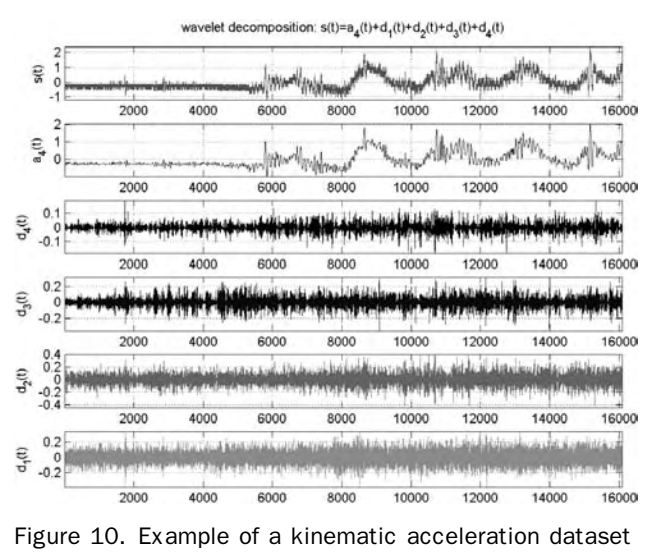

Figure 10. Example of a kinematic acceleration dataset in X direction for IMU400CC at LOD = 4; notation corresponds to Equation 4.

To complete the example of LOD selection, Figure 10 illustrates the exact decomposition procedure, described by Equation 4, up to four levels of decomposition for a kinematic dataset (removed noise statistics presented in Figure 9). The corresponding auto-correlation sequence (ACS) and power spectral density (PSD) of the removed noise, based on LOD = 4 for the same kinematic dataset are shown in Figure 11. Clearly, both ACS and PSD of the removed noise exhibit white noise characteristics (i.e., short correlation time and the maximum energy at high frequencies) indicating a good denoising performance.

The Effects of the IMU Signal De-noising on Initial Static Alignment

To assess the potential of improving the initial alignment of IMU sensors as a function of LOD, wavelet de-noising was

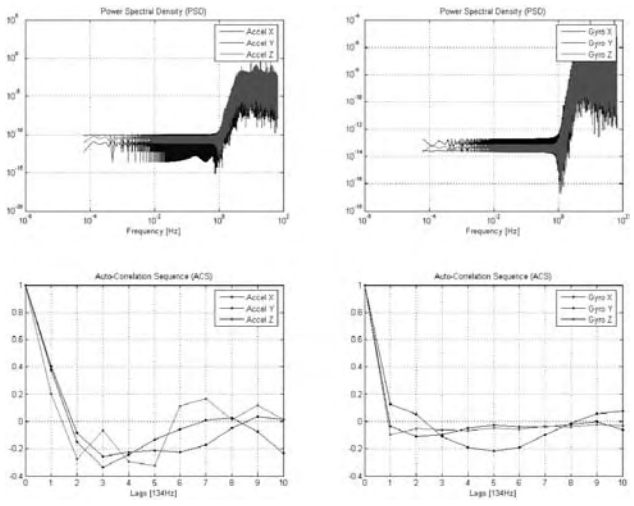

Figure 11. Power spectral density (PSD) and auto-correlation sequence of the removed noise for a kinematic IMU400CC dataset at LOD = 4.

TABLE 5. INITIAL HEADING ALIGNMENT DETERMINATION OF THE IMU400CC AS A FUNCTION OF WAVELET LOD USING A 370-SECOND STATIC DATASET

	Heading (°)	
LOD	Mean (μ)	Std (σ)
0	−177.72	11.56
1	−177.72	11.52
2	−177.73	11.48
3	−177.74	11.42
4	−177.72	11.39
5	−177.76	11.18
6	−177.76	10.99
7	−177.74	10.09
8	−177.72	8.18
9	−177.63	6.87
10	−177.41	5.95
11	−176.99	5.61
12	−176.13	7.44
13	−174.54	9.76
14	−170.84	13.67
15	−166.81	16.52
LN-100 (reference)	−176.24	

applied to a static IMU400CC dataset with a sampling rate of 100 Hz. The initial coarse alignment algorithm that determines the initial directional cosine transformation matrix is shown in Equations 5 and 6; see (Jekeli, 2001, p. 243). Using Equation 6, the initial attitude was determined as an average, based on a total of 370 seconds of static data, using a 1-second data averaged from 134 measurements (i.e., 134 Hz sampling rate). The LN-100 dataset was used as a reference truth, as both sensor axes were aligned according to the manufacturers' specification. As an example, the mean and the standard deviation of heading are shown in Table 5. It is important to point out that the estimation of the initial attitude is affected not only by the signal noise, but also by the instrumental biases. Thus, the relatively large epoch-to-epoch variations of the initial attitude estimates observed in this example (as evidenced by significant standard deviations listed in Table 5) can be attributed to the low quality of the MEMS IMU tested.

$$\mathbf{C}_{\mathbf{b}}^{\mathbf{a}} = \begin{bmatrix} 0 & 0 & -\bar{g} \\ \omega_e \cos\phi & 0 & -\omega_e \sin\phi \\ 0 & \bar{g}\omega_e \cos\phi & 0 \end{bmatrix}^{-1} \begin{bmatrix} (\mathbf{f}_{ib}^{b})^T \\ (\omega_{ib}^{b})^T \\ -(\mathbf{f}_{ib}^{b} \times \omega_{ib}^{b})^T \end{bmatrix} = \begin{bmatrix} c_{11} & c_{12} & c_{12} \\ c_{21} & c_{22} & c_{23} \\ c_{31} & c_{32} & c_{33} \end{bmatrix} \quad (5)$$

Where the heading (H), pitch (P) and roll (R) can be derived from Equations 6 a, b, and c, respectively.

$$H = \tan^{-1}\left(\frac{c_{21}}{c_{11}}\right) \quad \text{a)} \qquad P = \sin^{-1}(-c_{31}) \quad \text{b)} \qquad R = \tan^{-1}\left(\frac{c_{32}}{c_{33}}\right) \quad \text{c)} \quad (6)$$

Based on the analysis of Table 5, LOD = 11 seems to provide the best solution, in terms of the smallest standard deviation. The difference between this solution and heading provided by a precision alignment of LN-100 was 0.75°. It should be mentioned, however, that the smallest difference between the IMU400CC and LN-100 solutions was obtained for LOD = 12; though, the standard deviation in this case was bigger, as compared to the solution corresponding to LOD = 11.

The Effects of the IMU Signal Denoising on the Kinematic Navigation Solution

To further investigate the effect of the wavelet de-noising technique and the need for an optimal LOD selection in real kinematic situations, five free inertial navigation solutions using the IMU400CC data of moderate dynamics after LOD of 0, 1, 2, 3, and 4, respectively, were obtained by simulating GPS gaps following sufficient initial calibration of the inertial errors. The positional deviations of these solutions for

TABLE 6. IMU400CC POSITION DEVIATION WITH RESPECT TO THE REFERENCE GPS/INS TRAJECTORY WITH NO GPS GAPS, FOR DIFFERENT LEVELS OF LOD APPLIED TO IMU400CC DATA WITH SIMULATED GPS GAPS

		10 sec [m]		30 sec [m]		60 sec [m]		120 sec [m]	
Level of LOD		Mean	Std	Mean	Std	Mean	Std	Mean	Std
0	N	5.42	5.03	47.70	44.75	168.89	142.52	515.48	402.47
	E	2.96	2.75	32.20	33.17	201.44	218.67	1423.45	1587.30
	U	0.34	0.40	2.08	1.43	2.30	1.47	62.18	91.82
1	N	0.45	0.29	0.66	0.46	32.31	48.15	98.08	88.98
	E	0.13	0.16	4.00	4.14	16.92	18.81	208.48	252.87
	U	0.29	0.36	1.22	0.91	14.85	18.35	60.17	51.15
2	N	3.29	2.99	34.59	36.09	225.36	243.78	1048.14	962.52
	E	1.22	1.10	6.67	4.84	59.66	93.48	803.31	958.24
	U	0.30	0.36	1.44	1.02	2.30	2.20	58.93	76.56

different durations of the free inertial navigation (10, 30, 60 120 seconds) with respect to a high-end GPS/INS solution without GPS gaps (true reference) are listed in Table 6. After applying LOD = 1 to the IMU data, the navigation solution improved, as compared to the solution without signal denoising. The navigation solution with LOD = 2 degraded with respect to that of LOD = 1, while it was still better than the coordinates derived from the raw data. Thus, LOD = 1 is considered optimal for this experiment. However, as can be observed in Table 6, not all the IMU channels are affected uniformly; for example, the vertical coordinate is better for LOD = 2 (as compared to LOD = 1) for longer gaps. More testing is needed to analyze the LOD levels for varying dynamics, different data sampling rates and GPS gap duration.

Testing the Stochastic Properties of the IMU Sensors

A general form of a gyro (or accelerometer) measurement model consists of the following components (IEEE, Std 952–1997):

- a mathematical statement of the physical model,
- an error model consisting of a perturbation model and environmental sensitivities,
- a stochastic model describing random drift behavior, and
- a measurement model consisting of a linear combination of the output and additive measurement noise.

The physical model is normally described by differential or algebraic equations that define the physics of its operation. This is the deterministic part of the model, normally determined by dynamic modeling. Dynamic modeling of an optical gyro, for example, involves a scale factor, bias and misalignment, and environmental biases (IEEE, Std. 952–1997). The part of the general model that is of interest here is the stochastic model, which should be optimized to allow evaluation and improvement of the system's performance. This means that through optimal filtering the system errors could be reduced, leaving (ultimately) only the white noise. Therefore, careful estimation of the stochastic models for IMU sensors is crucial, and should be performed to achieve the highest navigation accuracy.

In general, for linear time-invariant systems with white noise inputs, it is possible to derive the stochastic model based on the system's output, using either time or frequency domain methods. Several methods in frequency and time domains have been devised for stochastic modeling. The two most commonly used techniques are: (a) the power spectral density (PSD) approach in the frequency domain, and (b) the Allan variance (or modified Allan variance) approach in the time domain. Other frequently used approaches are the adaptive Kalman filtering, and the correlation method. The correlation approach analyzes the autocovariance sequence computed from the output data to derive stochastic model parameters. In this case, the autocovariance can be modeled as a sum of exponentials and damped sinusoids, or can be expressed as coefficients of a difference equation, expressed as an autoregressive moving average (ARMA) process. It should be mentioned that the correlation methods are considered very model-sensitive, and are not suited to handling odd power processes, higher order processes or wide dynamic ranges. According to (IEEE, Std. 952–1997), Alan variance (or modified Allan variance) and PSD methods are the preferred techniques for the IMU stochastic error modeling. An example analysis of the sensor errors using the Alan variance method is presented in this paper.

Stochastic Error Modeling with Alan Variance: Overview

The Allan variance (Allan, 1966) is a method of representing RMS random drift error as a function of averaging time (IEEE, Std. 952–1997), and is defined as one half of the mean value of the square of the difference of adjacent time averages from a time series (Equation 8).

$$\sigma^2(\tau) = \frac{1}{2}\langle(\Delta\bar{y})^2\rangle \tag{8}$$

where $\sigma^2(\tau)$ is the Allan variance, n is the total number of original sample data y, τ_0 is the sample interval of the original data, $\tau = k\tau_0$, $k \leq \frac{(n-1)}{2}$ is the sample interval of the averaged grouped data, $\bar{y}$, formed using k consecutive original data, and $\langle\ \rangle$ represents the expectation operation, which can be replaced using the ensemble average.

The major stochastic noise contributors to the accelerometer and gyroscope data include: (a) gyro rate ramp (trend) defined as a gyro behaviour characterized by quadratic growth with the average time of the rate Allan variance, (b) gyro rate (acceleration) random walk defined as the drift rate error (acceleration) build-up with time that is due to white noise in angular acceleration (jerk), typically expressed in [°/h/h$^{1/2}$] ([m/s^2/h$^{1/2}$]), (c) flicker noise (bias instability), defined as random variation in bias, computed over specified finite sample time and averaging time intervals; it is a non-stationary process characterized by a 1/f PSD (the frequency domain equivalent to the second term of the Allan variance), typically expressed in [°/h] for gyros and [m/s^2, g] for accelerometers, respectively, (d) angle (velocity) random walk due to the white noise of gyroscope angular rate (acceleration) data, typically expressed as [°/h$^{1/2}$] (m/s/h$^{1/2}$), (e) quantization noise, defined as random variation in the digitized output signal due to sampling and quantizing of a continuous signal with a finite word length conversion, (f) exponentially correlated (Markov) noise characterized by an exponential decaying function with a finite correlation time, and (g) sinusoidal noise characterized by one or more distinct frequencies (IEEE Std. 952–1997 and IEEE Std. 528–2001). Generally, any combination of these processes can be present in the data, and different noise terms may appear in different regions of time scale τ.

Assuming that all random processes existing in the data are statistically independent, the Allan variance at any given τ is the sum of Allan variances due to individual random processes at the same τ (see Equation 9).

$$\sigma^2(\tau) = \frac{R^2\tau^2}{2} + \frac{K^2\tau}{3} + \frac{B^2 2\ln 2}{\pi} + \frac{N^2}{\tau} + \frac{3Q^2}{\tau^2} \tag{9}$$

where: $\sigma^2(\tau)$ is the Allan variance, first term represents the rate ramp, second term represents the rate random walk, the third one is the bias instability, the fourth term is the angle (velocity) random walk, and the last term is the quantization noise.

Stochastic Error Modeling with Alan Variance: Example

Eight hours of static data collected by H764G, HG1700 and IMU400CC were used to derive stochastic models for these IMU sensors, using the Allan variance approach. The IMU400CC data were first de-trended using an empirical 2nd order polynomial function representing the temperature-correlated deterministic error sources. The Allan variance plots were created for each IMU's accelerometer and gyroscope sensor, for τ ranging from 10^{-3} to 10^3 seconds. Example plots are shown in Figures 12a through f. The curves represent the empirical Allan variance in log-log representation, while the lines symbolize the linear fit corresponding to different error models, shown in Equation 9. Example interpretation of the analysis covering the full spectrum of the empirical Allan variance for one of the

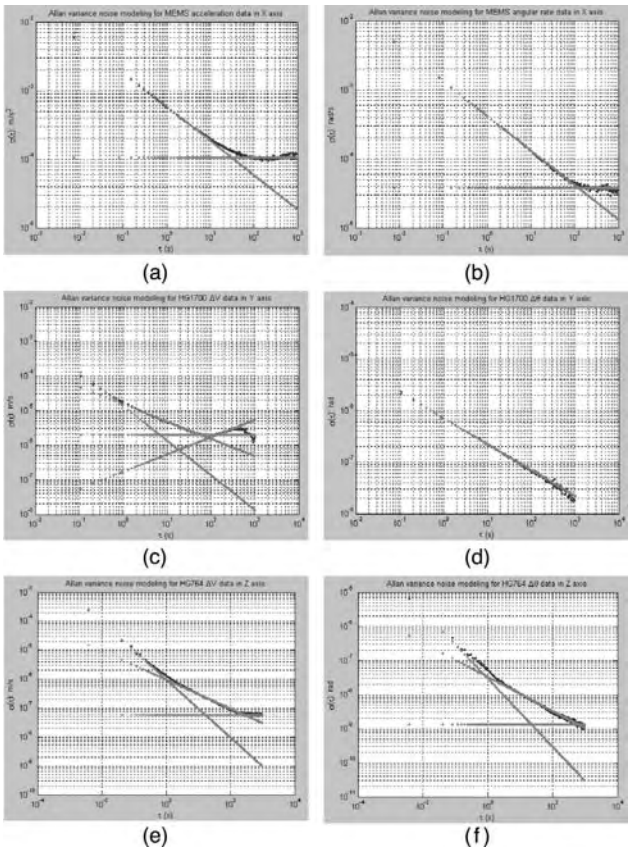

Figure 12. Allan variance estimations for various IMUs: (a) IMU400CC acceleration in *X* direction, (b) IMU400CC angular rate in *X* direction, (c) HG1700 delta velocity in *Y* direction, (d) HG1700 angular rate in *Y* direction, (e) H764G delta velocity in *Z* direction, (f) H764G angular rate in *Z* direction.

sensors, e.g., HG1700 gyroscope, indicates that the quantization noise dominates over the short times (less than 0.1 second), while the angle random walk dominates the remaining part of the time spectrum. The results of similar analyses for the rest of the IMU sensors are provided in Table 7.

The detailed noise characteristics for the three inertial sensors are listed in Table 7. In the current GPS/INS filter implementation, selected identified noise coefficients (e.g., the random walk coefficient ***N*** in Table 7) were used to form the stochastic noise model for the accelerometer and gyroscope bias drifts of the inertial sensors, as shown in Table 8. Since the bias instability coefficient, referred to as "B" in Table 7, reflects the best achievable stability of the sensor (Stockwell, 2004), the more conservative manufacturers' specifications were used in the Kalman filter (see Table 8). The coefficients from Table 7 for the same type of sensors (for example, all gyroscopes of HG1700) were averaged, and the units were converted to those used in the filter, resulting in the process noise (σ) listed in Table 8. For example, the three angular random walk coefficients for HG1700 are 0.0000815, 0.0000692 and 0.0000501 [rad/s/$s^{1/2}$], and their average is 0.0000669 [rad/s/$s^{1/2}$], approximated to 0.23 [°/$hr^{1/2}$]. Table 8 presents a summary of the error modeling applied in the GPS/INS Kalman filter for all tested sensors. It should be emphasized that this investigation is not complete yet, and more elaborated error models are currently explored, and the sensitivity of the navigation solution to the varying model characteristics is tested. The navigation results based on the models presented in this section are discussed next.

To demonstrate the improvement in the navigation solution due to the implementation of the derived error models, a 600-second GPS gap was introduced in a HG1700 dataset, and two free inertial navigation solutions were obtained: (a) using the Allan variance-based error models, and (b) using only the manufacturer's specification. Comparing to the true GPS/INS reference solution in Figure 13, an about 30 percent improvement can be found if the Allan variance-based error model is used.

TABLE 7. NOISE CONTRIBUTOR AND MODEL COEFFICIENTS ESTIMATED FROM THE LINEAR FIT TO THE EMPIRICAL ALLAN VARIANCE; FUNCTION ARGUMENTS 0, ½, 1, −½, −1 INDICATE THE SLOPE OF THE LINEAR FIT TO THE EMPIRICAL ALLAN VARIANCE (0 ≡ BIAS, ½ ≡ RATE RANDOM WALK, 1 ≡ RATE RAMP, −½ ≡ RANDOM WALK, −1 ≡ QUANTIZATION NOISE)

IMU	Sensor	R (1) [unit/s]	K (½) [unit/$s^{1/2}$]	B (0) [unit]	N (−½) [unit · $s^{1/2}$]	Q (−1) [unit · s]
H764G	Acc x	×	•	0.0000354	0.0000450	0.0002145
	Acc y	•	•	0.0000142	0.0000224	0.0002086
	Acc z	•	•	0.0000038	0.0000201	0.0001391
	Gyro x	×	×	×	0.0000003	0.0000045
	Gyro y	×	×	×	0.0000005	0.0000046
	Gyro z	×	×	×	0.0000005	0.0000057
HG1700	Acc x	•	•	0.0001074	0.0001820	0.0006204
	Acc y	•	•	0.0001000	0.0001303	0.0005917
	Acc z	•	•	0.0003268	0.0004521	0.0020290
	Gyro x	×	×	×	0.0000815	0.0000163
	Gyro y	×	×	×	0.0000692	0.0000115
	Gyro z	×	×	×	0.0000501	0.0000067
IMU400CC	Acc x	•	•	0.0002311	0.0004208	×
	Acc y	•	•	0.0002406	0.0004611	×
	Acc z	•	•	0.0013401	0.0004608	×
	Gyro x	•	•	0.0000540	0.0007868	×
	Gyro y	•	•	0.0000635	0.0007567	×
	Gyro z	•	•	0.0000752	0.0031097	×

Note: [unit ≡ m/s^2] for the acceleration data and [unit ≡ rad/s] for the gyro data; symbol (•) indicates that the effect attributed to this part of the empirical model exists in the corresponding sensor but the coefficients are not used here, and symbol (×) indicates that no effect for this part of the model is evidenced in the corresponding sensor.

TABLE 8. SUMMARY OF THE APPLIED INERTIAL SENSOR ERROR MODELING; LN-100 PARAMETERS WERE NOT DERIVED IN THIS STUDY (FOR REFERENCE TO LN100 PARAMETERS, SEE, GREJNER-BRZEZINSKA AND WANG, 1998)

	IMU Error Sources	Initial Conditions (σ)	Process Noise (σ)	Stochastic Model
LN-100	Accelerometer Scale Factor	40 ppm	0	Random Constant
	Accelerometer Bias Drift	25 μg	0.08 $\mu g \cdot hr^{1/2}$	Random Walk
	Gyroscope Scale Factor	1 ppm	0	Random Constant
	Gyroscope Bias Drift	0.003 °/hr	0.001 °/$h^{1/2}$	Random Walk
H764G	Accelerometer Scale Factor	100 ppm	0	Random Constant
	Accelerometer Bias Drift	25 μg	0.05 $\mu g \cdot hr^{1/2}$	Random Walk
	Gyroscope Scale Factor	5 ppm	0	Random Constant
	Gyroscope Bias Drift	0.0035 °/hr	0.0015 °/$hr^{1/2}$	Random Walk
HG1700	Accelerometer Scale Factor	300 ppm	0	Random Constant
	Accelerometer Bias Drift	1.0 mg	0.3 $\mu g \cdot hr^{1/2}$	Random Walk
	Gyroscope Scale Factor	150 ppm	0	Random Constant
	Gyroscope Bias Drift	2.0 °/hr	0.23 °/$hr^{1/2}$	Random Walk
MEMS IMU400CC	Accelerometer Scale Factor	1%	0	Random Constant
	Accelerometer Bias Drift	8.5 mg	0.8 $\mu g \cdot hr^{1/2}$	Random Walk
	Gyroscope Scale Factor	1%	0	Random Constant
	Gyroscope Bias Drift	1.0 °/sec	2.7°/$hr^{1/2}$	Random Walk
Other Error Sources	Velocity unmodeled error	1.0 m/sec	5 $\mu g/Hz^{1/2}$	Random Walk
	Attitude unmodeled error	(25, 5 5)° in H, P, R	0.001 °/$hr^{1/2}$	Random Walk
	Lever arm	0.05 m	0	Random Constant
	Gravity Error	25 μg	1st order Gauss-Markov process with 37 km correlation distance	

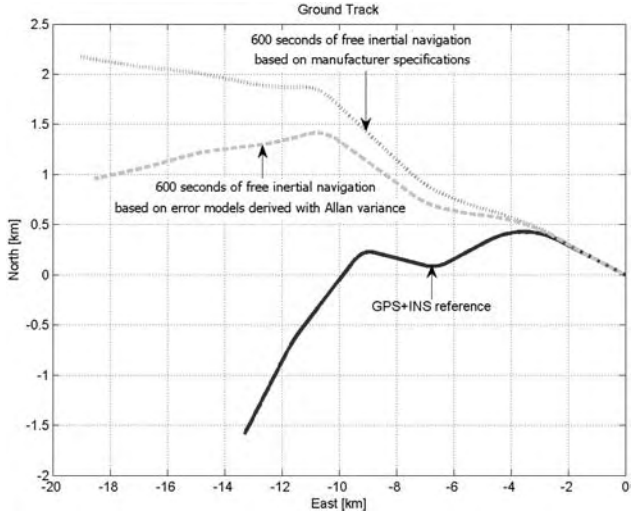

Figure 13. Reference GPS/INS navigation solution compared to the free navigation solution of HG1700 using (1) Allan variance-based error modeling, and (2) manufacturer specifications.

Navigation Results of Various IMU Sensors

As a summary, the combined effect of the three procedures discussed in this paper: extended gravity compensation, signal de-noising and the IMU error modeling, is now tested for different IMU categories. The cross-comparison of the IMU sensors provides important information for finding optimal georeferencing solutions, including the selection of sensor hardware and software, for various mapping applications and mission environments. The comprehensive analysis of this topic goes beyond the scope of this paper, thus, only a limited discussion is offered here to provide basic performance metrics.

To compare the performance of various IMU sensors, four trajectories obtained by free inertial navigation with four different IMU sensors, as listed in Table 9, were analyzed during five simulated GPS gaps (shown in Figure 1), at different locations and different dynamics. The first gap was introduced at low dynamics in an urban area, traveling NE, while the four remaining gaps were created at medium dynamics on the I-70 highway going EW. The GPS/INS solution based on LN-100 data, with continuous GPS update at 1Hz rate was used as positional reference, while each attitude solution was compared to the respective GPS/INS solution (i.e., using each analyzed IMU). Extended gravity compensation was applied to LN-100 and H764G, signal denoising was applied to IMU400CC data, and the error modeling for all sensors follows the characteristics presented in Tables 7 and 8. The average positioning and attitude errors for four different gaps (10, 30, 60, and 120 seconds) along with their standard deviations are listed in Tables 9 and 10. It can be observed in Tables 9 and 10 that different grades of IMUs performed quite differently, reflecting, in general, expected performance within each class of inertial sensors. It is noteworthy to mention that for a very short gap of 10 seconds, the differences among sensors are hardly visible, while longer periods exhibit substantial performance differences, as expected.

Conclusion

Direct orientation of mapping sensors has become the de-facto technology for land-based mobile mapping systems in recent years, and is rapidly gaining dominance in airborne applications. Mostly considered as a "black box" system, GPS/INS-based georeferencing solutions at different performance levels are available from a growing number of vendors. As the application base is increasing, the demand is growing to further improve the overall performance of such systems, as well as to provide support for applications with very specific requirements. In this paper, several methods aimed at incremental improvements of the performance of GPS/INS-based georeferencing systems were discussed. Our investigation targeted three particular areas to improve the georeferencing solution by using extended gravity compensation techniques, signal de-noising, and detailed, sensor-specific error modeling. A land-based mobile mapping system equipped with five different grade IMUs provided data for the tests and analyses presented here.

TABLE 9. POSITION ERROR (WITH RESPECT TO REFERENCE GPS/INS TRAJECTORY) AS A FUNCTION OF GPS GAP DURATION AT DIFFERENT VEHICLE DYNAMICS

		10 sec Low Dynamics		30 sec Moderate Dynamics		60 sec Moderate Dynamics		120 sec Moderate Dynamics	
		Mean	Std	Mean	Std	Mean	Std	Mean	Std
		[m]		[m]		[m]		[m]	
LN-100	N	0.02	0.02	0.09	0.06	0.22	0.15	0.57	0.41
	E	0.00	0.00	0.00	0.00	0.01	0.01	0.03	0.02
	U	0.00	0.00	0.01	0.01	0.04	0.04	0.23	0.25
H764G	N	0.00	0.00	0.01	0.01	0.04	0.04	0.20	0.20
	E	0.01	0.01	0.06	0.04	0.16	0.12	0.47	0.36
	U	0.00	0.00	0.02	0.02	0.08	0.07	0.23	0.17
HG1700	N	0.00	0.00	0.01	0.02	0.65	1.01	12.07	15.72
	E	0.03	0.03	0.33	0.33	1.55	1.49	8.86	9.59
	U	0.02	0.01	0.06	0.04	0.11	0.06	0.24	0.29
MEMS	N	0.45	0.29	0.66	0.46	32.31	48.15	98.08	88.98
	E	0.13	0.16	4.00	4.14	16.92	18.81	208.48	252.87
	U	0.29	0.36	1.22	0.91	14.85	18.35	60.17	51.15

TABLE 10. ATTITUDE ERROR (WITH RESPECT TO REFERENCE GPS/INS TRAJECTORY) AS A FUNCTION OF GPS GAP DURATION AT DIFFERENT VEHICLE DYNAMICS

		10 sec Low Dynamics		30 sec Moderate Dynamics		60 sec Moderate Dynamics		120 sec Moderate Dynamics	
		Mean	Std	Mean	Std	Mean	Std	Mean	Std
		[arcsec]		[arcsec]		[arcsec]		[arcsec]	
LN-100	H	0.05	0.03	0.42	0.33	0.63	0.32	0.71	0.24
	P	0.12	0.11	0.57	0.38	0.92	0.46	0.72	0.40
	R	0.99	0.64	2.20	1.02	2.50	0.81	2.46	0.59
H764G	H	0.42	0.25	0.68	0.24	0.74	0.18	0.76	0.13
	P	0.19	0.12	0.27	0.10	0.22	0.10	0.13	0.11
	R	0.28	0.16	0.57	0.27	0.81	0.32	0.94	0.26
HG1700	H	4.97	3.89	18.20	21.35	81.34	86.48	268.42	213.61
	P	0.25	0.14	0.48	0.24	0.36	0.25	0.99	0.96
	R	4.98	3.88	18.19	21.37	81.31	86.45	268.22	213.42
MEMS	H	19.66	16.97	91.22	68.85	249.47	194.32	703.25	513.21
	P	145.85	93.96	384.14	207.40	458.27	196.53	1206.31	1261.60
	R	13.85	10.93	147.64	149.68	617.54	555.61	1465.15	960.28

The test results presented here confirm that for high-end IMUs the introduction of the DOV data can improve the solution, mainly in the horizontal coordinates and attitude components. IMU signal de-noising is an important pre-processing step, essential for low-cost MEMS-based IMU systems. Our tests performed on consumer grade IMU confirmed that by appropriately selecting the level of signal decomposition, the free-INS navigation solution, as well as, the initial alignment show significant improvements.

The error modeling of the IMU sensors, in general, is a very complex task. Our investigation was focused on deriving stochastic models of the IMU sensors with the Allan variance method. Using the test data, we successfully estimated error models for three different grade IMUs. As an example of the effect of these models on the navigation results, an about 30 percent improvement in free navigation mode was demonstrated for the HG1700 IMU. Subsequently, this information was used in the fine-tuning of the models used in the Kalman filtering process. This investigation is still underway and more comprehensive analyses will be provided in the subsequent publication.

The initial test results obtained according to the three proposed procedures of incremental improvements in the GPS/INS navigation results confirmed that these improvements are in fact feasible. The introduction of these techniques could result in better long-term performance and/or higher accuracy. The effectiveness of the three methods is a function of the IMU grade, and thus, not all the sensor will equally benefit from each proposed technique. Still, the cross-comparison of various grade IMU sensors provided valuable data for land-based mobile mapping systems, where the performance of the free inertial solution is important. Additional research is expected to assess and analyze the performance impact of the three techniques on the more dynamic airborne platform.

Acknowledgments

The authors would like to thank Dr. Jay Kwon for his helpful comments on the manuscript and for running his navigation simulator used to create Table 3.

References

Abdullah, Q., 1997. Evaluation of GPS-inertial navigation system for airborne photogrammetry, presented at the 1997 ACSM/ASPRS Annual Convention and Exposition, 07–10 April, Seattle, Washington.

Allan, D.W. 1966. Statistics of atomic frequency standards, *Proceedings of the IEEE*, Vol. 54, No. 2, pp. 221–230.

Bossler, J.D., and C., Toth, 1995. Accuracies obtained by the GPSVan™, *Proceedings of GIS/LIS'95*, Vol. 1, pp. 70–77.

Bossler, J.D., C. Goad, P. Johnson, and K. Novak, 1991. GPS and GIS map the nation's highway, *GeoInfo System Magazine*, March, pp. 26–37.

El-Sheimy, N., and K.P. Schwarz, 1999. Navigating urban areas by VISAT – a mobile mapping system integrating GPS/INS/digital cameras for GIS application, *Navigation*, Vol. 45, No. 4:275–286.

El-Sheimy, N., K.P. Schwarz, M. Gravel, 1995. Mobile 3-D positioning psing GPS/INS/video cameras, *Proceedings of the Mobile Mapping Symposium*, OSU Center for Mapping, pp. 236–249.

Gleason, D.M., 1992. Extracting gravity vectors from the integration of global positioning system and inertial navigation system data, *Journal of Geophysical Research*, Vol. 97(B6), 1992:8853–8864.

Grejner-Brzezinska, D., Y. Yi, C. Toth, R. Anderson, J. Davenport, D. Kopcha, and R. Salman, 2003. Enhanced gravity compensation for improved inertial navigation accuracy, *Proceedings of the ION GPS/GNSS*, 09–12 September, Portland, Oregon, CD ROM, pp. 2899–2909.

Grejner-Brzezinska, D.A., Y. Yi, C. Toth, R. Anderson, J. Davenport, D. Kopcha, and R. Salman, 2004a. On improved gravity modeling supporting direct georeferencing of multisensor systems, *Proceedings of the XXth ISPRS Congress*, Istanbul, Turkey, 12–23 July 2004, unpaginated CD ROM.

Grejner-Brzezinska, D., Y. Yi, C. Toth, R. Anderson, J. Davenport, D. Kopcha, and R. Salman, 2004b. On the improved gravity compensation in inertial navigation, *Photogrammetirc Engineering & Remote Sensin*g, Vol. 70, No. 6:663–664.

Grejner-Brzezinska, D.A., Y. Yi, and C.K. Toth, 2001. Bridging GPS gaps in urban canyons: benefits of ZUPT, *Navigation*, Vol. 48, No. 4, Winter 2001–2002: 217–225.

Grejner-Brzezinska, D., 2001. Mobile mapping technology: ten years later, part II, *Surveying and Land Information Systems*, Vol. 61, No. 3:83–100.

Grejner-Brzezinska, D.A., 1999. Direct exterior orientation of airborne imagery with GPS/INS system: performance analysis, *Navigation*, Vol. 46, No. 4:261–270.

Grejner-Brzezinska, D.A., and Wang J., 1998. Gravity modeling for high-accuracy GPS/INS integration, *Navigation*, Vol. 45, No. 3: 209–220.

Grejner-Brzezinska, D.A., 1997. High accuracy airborne integrated mapping system, *Advances in Positioning and Reference Frames* (F.K. Brunner, editor), IAG Scientific Assembly, Rio De Janeiro, Brazil, 03–09 September, Springer, pp. 337–342.

IEEE, 1997. IEEE Standard 952–1997, IEEE Standard Specification Format Guide and Test Procedure for Single-Axis Interferometric Fiber Optic Gyros.

IEEE, 2001. IEEE Standard 528–2001, IEEE Standard for Inertial Sensor terminology, IEEE Aerospace and Electronic Systems Society, sponsored by the Gyro and Accelerometer Panel.

Li, X.P., and C. Jekeli, 2004. Improving resolution of airborne gravimetric system by using of wavelets shrinkage de-noising, *Proceedings of the ION Annual Meeting*, Dayton, Ohio, 07–09 June, CD ROM, pp. 491–496.

Jekeli, C., 2001. *Inertial Navigation Systems with Geodetic Applications*, deGruyter, Berlin/New York.

Jekeli, C., 1997. The effect of earth's gravity on precise, short-term, 3-D free-inertial navigation, *Navigation*, Vol. 44, No. 3:347–357.

Kwon, J.H., 2004. Gravity Compensation Methods for Precision INS, *Proceedings of the ION Annual Meeting*, Dayton, Ohio, 07–09 June, CD ROM, pp. 483–490.

Mostafa, M., 2002. Camera/IMU Boresight Calibration: New Advances and Performance Analysis, *Proceedings of the ASPRS Annual Meeting*, Washington, DC, April 21–26 2002, unpaginated CD ROM.

Mostafa, M., and J. Hutton, 2001. Airborne Kinematic Positioning and Attitude Determination Without Base Stations, *Proceedings of the International Symposium on Kinematic Systems in Geodesy, Geomatics, and Navigation (KIS 2001)*, Banff, Canada, 04–08 June, unpaginated CD ROM.

Mostafa, M., J. Hutton, and E. Lithopoulos, 2000. Ground accuracy from directly georeferenced imagery, *GIM International*, Vol.14 No.12, pp. 38–41.

Schwarz, K.P., M.A. Chapman, M.E. Cannon, and P. Gong, 1993. An integrated INS/GPS approach to the georeferencing of remotely sensed data, *Photogrammetric Engineering & Remote Sensing*, 59(11):1167–1674.

Skaloud, Jan, 2002. Direct Georeferencing in Aerial Photogrammetric Mapping, *Photogrammetric Engineering & Remote Sensing*, 68(3):207–210.

Skaloud, J., M. Cramer, and K.P. Schwarz, 1996. Exterior orientation by direct measurement of camera position and attitude, *International Archives of Photogrammetry and Remote Sensing*, Vol. XXXI, Part B3:125–130.

Stockwell, W., 2004. Bias Stability Measurement: Allan Variance, URL: *http://www.xbow.com/Support/Support_pdf_files/Bias_Stability_Measurement.pdf*, last date accessed 27 January 2005.

Toth C., D.A. Grejner-Brzezinska, 1998. Performance analysis of the airborne integrated mapping system (AIMS™), *ISPRS Commission II Symposium on Data Integration: Systems and Techniques*, 13–17 July, Cambridge, England: 320–326.